

Optical lattice quantum simulator of dynamics beyond Born-Oppenheimer

Javier Argüello-Luengo,^{1,*} Alejandro González-Tudela,^{2,†} and J. Ignacio Cirac^{3,4}

¹*Departament de Física, Universitat Politècnica de Catalunya, Campus Nord B4-B5, 08034 Barcelona, Spain*

²*Institute of Fundamental Physics IFF-CSIC, Calle Serrano 113b, 28006 Madrid, Spain.*

³*Max-Planck-Institut für Quantenoptik, Hans-Kopfermann-Str. 1, 85748 Garching, Germany*

⁴*Munich Center for Quantum Science and Technology (MCQST), Schellingstr. 4, 80799 Mchen, Germany*

Here, we propose a platform based on ultra-cold fermionic molecules trapped in optical lattices to simulate nonadiabatic effects as they appear in certain molecular dynamical problems. The idea consists in a judicious choice of two rotational states as the simulated electronic or nuclear degrees of freedom, in which their dipolar interactions induce the required attractive or repulsive interactions between them. We benchmark our proposal by studying the scattering of an electron or a proton against a hydrogen atom, showing the effect of electronic exchange and inelastic ionization as the mass ratio between the simulated nuclei and electrons— a tunable experimental parameter in our simulator— becomes comparable. These benchmarks illustrate how the simulator can qualitatively emulate phenomena like those appearing in molecular dynamical problems even if the simulated interaction occurs in two-dimensions with a dipolar scaling. Beyond the molecular implementation proposed here, our proposal can be readily extrapolated to other atomic platforms, e.g., based on fermionic Rydberg atoms.

Cold atomic systems in optical lattices have been one of the leading platforms to simulate quantum many-body physics over the past two decades [1, 2]. Their combination of exceptional control [3] and detection techniques [4] have enabled the study of relevant many-body phenomena in condensed matter [5–19] or lattice high-energy physics problems [20–22]. Recently, a new avenue has opened in optical lattice setups with the proposals to simulate few-body problems [23–26] akin to those appearing in quantum chemistry, but with different interaction scalings and dimensionalities. Compared to other trapped ion simulator proposals [27–31], these optical lattice simulators natively encode the electronic degrees of freedom in the fermionic atoms hopping along the lattice, which combined with quantum gas microscopes enables unique capabilities for the detection of electronic correlations. However, these atomic proposals have several limitations. First, they focus on the exploration of ground state physics rather than dynamical properties [23–26], where these analogue simulators manifest their full potential. Second, they emulate their required interactions either by extending the range of the local on-site interactions through complex laser-assisted processes [23–25] or by harnessing Rydberg forces, which are both short-range and limited by spontaneous emission [26]. Last, and most important, the nuclei are emulated as classical, fixed potentials, and thus cannot capture nonadiabatic dynamical effects.

In this Letter, we propose a new strategy that overcome the aforementioned limitations by harnessing recent advances for molecules trapped in an optical lattice. By using two dressed rotational levels, the system incorporates both the electronic and nuclear degrees of freedom as dynamical variables, thus providing a platform to explore a broader class of quantum effects beyond the constraints of the Born-Oppenheimer approxi-

mation. Importantly, we show that by adding an external electric field, there exists a regime where the dipolar interactions between these molecular states can emulate the repulsive nucleus-nucleus and electron-electron interactions, while at the same time yielding attractive nucleus-electron forces between the different levels. To benchmark the simulator, we illustrate how it can emulate the scattering of an electron or proton (H^+) against a hydrogen atom (H), showing how to prepare the initial scattering wavepackets and extract the resulting scattering cross-section. Importantly, we show that the proposed simulator can access the nonadiabatic regime due to the ability to tune the effective nucleus vs. electron mass ratio experimentally,

Complete quantum-chemistry Hamiltonian.— The simulation of molecular problems starts by choosing an appropriate basis to write the second-quantized quantum chemistry Hamiltonian. A natural choice for cold-atom simulators is the grid discretized basis, where one chooses one fermionic mode per point of space and degree of freedom. Compared to Refs. [23–26], focused on the electronic system, here we also need to include additional operators to account for the nuclear degrees of freedom. The final complete chemistry Hamiltonian we aim to simulate reads:

$$\hat{H} = - \sum_{\alpha} J_{\alpha} \sum_{\langle i,j \rangle} \hat{c}_{\alpha i}^{\dagger} \hat{c}_{\alpha j} - J_e \sum_{\sigma, \langle i,j \rangle} \hat{f}_{\sigma i}^{\dagger} \hat{f}_{\sigma j} + \sum_{i,j} V_{i,j} \left[\sum_{\sigma, \sigma'} \hat{n}_{\sigma i}^f \hat{n}_{\sigma' j}^f + \sum_{\sigma, \alpha} Z_{\alpha} \hat{n}_{\alpha i}^c \hat{n}_{\sigma j}^f - \sum_{\alpha \neq \alpha'} Z_{\alpha} Z_{\alpha'} \hat{n}_{\alpha i}^c \hat{n}_{\alpha' j}^c \right], \quad (1)$$

where $\hat{c}_{\alpha i}^{(\dagger)}$ is the annihilation (creation) operator of nucleus α at site \mathbf{i} , and $\hat{f}_{\sigma i}^{(\dagger)}$ are the ones of fermions with spin σ . $\hat{n}_{\sigma i}^f = \hat{f}_{\sigma i}^{\dagger} \hat{f}_{\sigma i}$ and $\hat{n}_{\alpha i}^c = \hat{c}_{\alpha i}^{\dagger} \hat{c}_{\alpha i}$ are the electronic

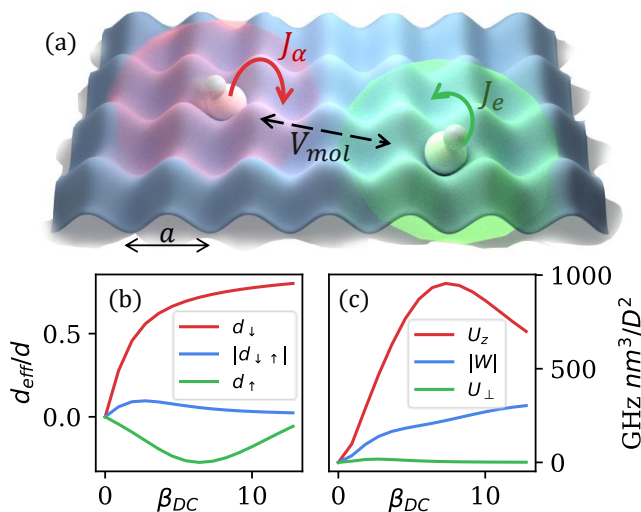


Figure 1. (a) Scheme of the simulator, where molecules in two different rotational levels $|\downarrow\rangle$ and $|\uparrow\rangle$ (represented in red and green along the text) tunnel in an optical lattice with rates J_α and J_e , playing the role of nuclei and electrons, respectively. The dipolar interactions between these molecular levels satisfy the desired attractive and repulsive nature of the simulated long-range forces. (b) Effective dipolar moment of rotational levels $|\downarrow\rangle = |00\rangle$ and $|\uparrow\rangle = |20\rangle$, as well as the overlap $d_{\downarrow\uparrow} = \langle\downarrow|\hat{d}_0|\uparrow\rangle$ for different values of external DC field (see main text). (c) Components of the resulting spin Hamiltonian of Eq. (2) for increasing values of the electric field.

and nuclear number operators, respectively. The first line in Eq. (1) represents the kinetic term, where J_α and J_e are the hopping amplitudes for nucleus α and the electronic degrees of freedom, respectively. The terms in brackets indicate the extended interaction among electrons and nuclei, which are weighted by their charge number, Z_α . Inspired by this Hamiltonian, in the following, we propose a two-dimensional model that exhibits an extended interaction $V_{i,j} = V_{\text{mol}}(|\mathbf{i} - \mathbf{j}|)$ with the correct signs, so that the simulated nuclei and electrons repel themselves, but are attracted to each other.

Simulator setup.— A general scheme of the setup is depicted in Fig. 1(a): individual molecules are trapped at the minima of a two-dimensional optical lattice with spacing a and $N_{x,y}$ sites per side [32–34]. An important aspect is that, for m different types of nuclei involved in the simulation, the chosen molecule must have $m + 2$ internal levels that encode the nuclear and electronic degrees of freedom of the molecular Hamiltonian of Eq. (1). For now, we focus on one electronic spin component and assume that all nuclei are of the same type, so that nuclear and electronic creation operators, \hat{c} and \hat{f} , only require access to two rotational levels.

A crucial aspect of this simulator is the choice of rotational levels, ensuring repulsion when molecules are in the same state and attraction when in different states. For that, one can choose $^1\Sigma$ polar molecules [35], where

there are no unpaired electrons, and the electronic wavefunction is invariant under all symmetry transformations, as there is neither orbital nor spin angular momentum [36]. These molecules have well-isolated internal rotational levels $|N, M\rangle$ [37], in which the first index denotes the rotational angular momentum quantum number associated to \mathbf{N}^2 , and the second one is its projection along the quantization axis. In the absence of fields, these energy levels are $(2N + 1)$ -fold degenerate, since the molecules are described by an effective rigid-rotor Hamiltonian $\hat{H}_{\text{rot}} = B_N \mathbf{N}^2$, where B_N is the rotational constant. To break this degeneracy, we add an external DC field, $\hat{H}_{\text{DC}} = -\mathbf{d} \cdot \mathbf{E}_{\text{DC}} = -\hat{d}_z E_0$, that renormalizes its effective dipole moment. This field is aligned along the z -axis to preserve the isotropy of the simulation over the optical lattice situated in the XY plane. As a result, the lowest rotational state, $|00\rangle \equiv |\downarrow\rangle$, which would otherwise be rotationally symmetric in the absence of fields, acquires an effective positive dipolar moment $d_\downarrow = \langle\downarrow|\hat{d}_0|\downarrow\rangle$, as shown in Fig. 1(b). Other states, like $|20\rangle \equiv |\uparrow\rangle$, antialigns with the field at intermediate values $\beta_{\text{DC}} \equiv E_0 d / B_N \sim 1$, as also shown in Fig. 1(b), which enables to induce an attractive interaction between molecules when they are in these different states. This can be explicitly shown by projecting the dipolar interaction Hamiltonian onto the reduced subspace formed by these two states [36]:

$$V_{i,j} = \frac{1}{|\mathbf{r}_i - \mathbf{r}_j|^3} \left[\frac{U_\perp}{2} (\hat{S}_i^+ \hat{S}_j^- + \text{h.c.}) + U_z \hat{S}_i^z \hat{S}_j^z + W (\hat{S}_i^z + \hat{S}_j^z) \right], \quad (2)$$

where $U_\perp \equiv 2d_{\downarrow\uparrow}^2$, $U_z \equiv (d_\uparrow - d_\downarrow)^2$, and $W \equiv (d_\uparrow^2 - d_\downarrow^2)/2$ [36–40]. Here, $d_\sigma = \langle\sigma|\hat{d}_0|\sigma\rangle$, and $d_{\downarrow\uparrow} = \langle\uparrow|\hat{d}_0|\downarrow\rangle$ are the projections of the dipole operator in the rotational subspace $\{|\downarrow\rangle, |\uparrow\rangle\}$ where the spin operators \hat{S}_i are defined. In Fig. 1(c), we plot these parameters (U_z, W, U_\perp) for increasing values of the electric field. There, we observe how for $\beta_{\text{DC}} \approx 8$, state-of-the-art lattice spacings $a \sim 500$ nm, and permanent dipole moments $d \sim 1$ Debye (as is the case for molecules such as KRb or NaRb [32, 41]), one obtains a nearest-neighbor value $V_0 = U_z/a^3 \sim 10$ kHz, which is in the order of the tunneling time. In addition, we find that the detrimental mixing between rotational states is reduced to $U_\perp/U_z \sim 1\%$. The latter term, W , corrects the strength of these interactions but does not change their scaling. As a result, one is left to this order with an effective Hamiltonian that is diagonal in the z -basis where molecules on the same state experience a repulsive interaction due to the alignment of their charges, while different states attract each other. In both cases, we will consider an interaction of the form $V_{\text{mol}}(r) = V_0 a^3 / (r_0^3 + r^3)$, which captures both the $1/r^3$ scaling of dipolar interactions and the renormalization at short distances, $r_0 \sim a$, associ-

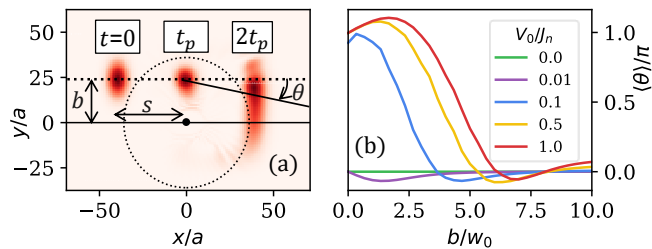


Figure 2. (a) Temporal evolution of a 2D wavepacket of width $w_0/a = 4$ that propagates in the right direction (dotted line) with carrier wavevector $k_0a = \pi/2$ for a lattice with 140×120 sites, $b/w_0 = 1.5$ and $V_0/J_n = 0.4$. The initial horizontal separation is $s/a = 40$ sites. The Mie potential that emulates the nucleus is centered at the origin and the dotted circumference indicates a radius $r_M/a = 36$. (b) Expected scattering angle as a function of the impact parameters of different strengths.

ated to on-site interactions [42]. Although it differs from the $1/r$ Coulomb potential that characterizes quantum chemistry, the induced two-dimensional extended forces encode the correct attractive and repulsive character of the interactions among electrons and nuclei. Relevantly, the presence of nuclear motion in the simulation allows one to access regimes where nonadiabatic effects appear. This is especially relevant for chemical reactions and scattering dynamics that are influenced by chirality [43] or the presence of exceptional points [44–47], where numerical methods based on the Born–Oppenheimer approximation are compromised. Given the difficulty to numerically tackle few-body problems in those regimes, in the following we will explore some simplified scenarios that we can numerically study in detail to validate and characterize the simulator, guiding the initial configurations for the experimental exploration of this field.

Simulating single-particle scattering.— We first start benchmarking the simulator by studying its potential to emulate classical scattering processes. For that, we consider a single dynamical *projectile* (a proton or electron, represented by the corresponding rotational level of a molecule) against a fixed classical *target* described by a Mie potential of the form $V_{\text{Mie}}(r, r_M) = V_0 [(r/r_M)^{-2} - 2(r/r_M)^{-1}]$, which is repulsive at short distances, $r \ll r_M$, and exhibits an attractive quadratic local minimum at distance r_M . In an experiment, this fixed potential can be easily engineered with an optical potential defined, e.g., by an intensity phase mask [48].

The projectile is prepared as a gaussian wavepacket $\psi_{w_0, k_0}(\mathbf{r})$ whose initial width w_0 extends over several sites of the lattice and carries initial momentum k_0 along the horizontal axis [49]. It has an initial horizontal separation s from the central potential, which is reached maximally at time $t_p = s/(2Ja)$. Using cold atoms, the amplitude of this wavepacket can be prepared with the expansion of a localized state [50–52], and the correct phase can be

spatially imprinted using light-modulation [53, 54] or the reflection with barrier potentials [55]. In two dimensions, this moving wavepacket would however suffer from an undesired dispersion along the vertical axis, which results into an additional width $w(t)$ and quadratic phase $\varphi(\mathbf{r}, t)$ that increase as the projectile propagates (see [49]). To reduce this distortion at impact time t_p , here we propose a different strategy by initially preparing the wavepacket $\psi_{\text{in}}(\mathbf{r}, 0) = \psi_{w(t_p), k_0}(\mathbf{r}) \exp[-i\varphi(\mathbf{r}, t_p)]$, which dynamically compensates for these effects so that the target is reached by an undistorted gaussian state.

In Fig. 2(a) we superpose the probability density, $|\psi_{\text{in}}(\mathbf{r}, t)|^2$, of three different instants in the scattering of this self-focusing wavepacket. For an *impact factor* (vertical separation) comparable to the length of the attractive region of the potential, $b \approx r_M$, one encounters the *glory impact factor* where the wavepacket maximally bends towards the center of the potential, as we can appreciate in the final frame. In Fig. 2(b), we calculate the average scattering angle $\langle \theta \rangle$ away from the incoming direction for increasing values of impact parameters. For direct collisions ($b = 0$) the wavepacket is scattered backwards due to the repulsive central region of the potential [$\langle \theta \rangle \approx \pi$]. As the scattering strength of the nuclear potential V_0/J_e increases, we observe that the most negative scattered angle appears for larger glory impact parameters.

Simulating electron exchange.— We now study the electron exchange when a proton impacts a hydrogen atom, as schematized in Fig. 3(a,b). For the numerical benchmark presented here, we consider a dynamical proton scattering against a dynamical electron bounded to a fixed nuclear potential $V_{\text{mol}}(r)$, which can be fixed optically in an experiment. One should note that the ratio between effective incoming kinetic energy $K_p = 2J_n(1 - \cos k_0a)$ and the ionization energy of the target hydrogen, I , can be controlled through the carrier wavevector k_0 , or the nuclear dynamics $J_n < J_e$. To minimize diffusive processes along the projectile direction, we choose the linear region of the dispersion relation $k_0a = \pi/2$, which still allows us to tune $K_p = 2J_n$, through the nuclear tunneling rate J_n . As the electron in the target hydrogen feels the attraction of the incoming proton, it can be either released from its parent nucleus or become bounded to the propagating projectile after the scattering event. In Fig. 3(c) we illustrate the scattered states of the projectile at time $2t_p$, for the impact parameter $b/a = 3$ and $J_n/J_e = 0.022$, where we observe the presence of diffraction fringes in the final state due to interactions with the target. In momentum space [Fig. 3(d)], we observe a larger emission in the forward direction. Dashed circle indicates the initial carrier momentum k_0 , which highlights the reduced kinetic energy in the projectile due to the inelastic energy transfer to the electron in the target hydrogen. In Fig. 3(e), we show the horizontal spatial correlations between the scattered proton and target electron, which confirms that the

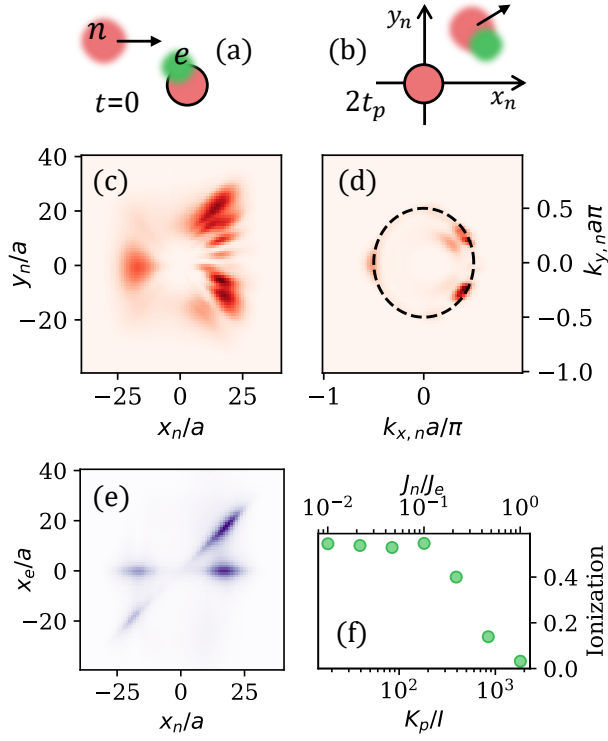


Figure 3. (a,b) Scheme for nuclear scattering against hydrogen at times 0 and $2t_p$, respectively. Blurry contours indicate that the incoming nucleus [n] and target electron [e] are treated quantum-mechanically, while the contoured nucleus is fixed. Nuclear probability density of the scattered nucleus in real (c) and momentum space (d). Dashed line indicates momentum $k_0 a = \pi/2$. (e) Spatial correlations between the scattered nucleus and the ejected electron along the axis parallel to the incoming nucleus (respectively). (f) Electronic excitation rate as a function of the tunneling rate of the incoming nuclear wavepacket. Parameters: $N_{x,y} = 80$, $V_0/J_e = 0.4$, $w_0/a = 3$, $r_0/a = 1.1$, $J_n/J_e = 0.022$, $k_0 a = \pi/2$, $b/a = 3$.

electron remains bound to the parent nucleus (horizontal correlation), or associates with the incoming projectile in an exchange process (diagonal correlation).

In a Born-Oppenheimer picture, for this electron exchange to occur, the process requires an exchange time comparable to the inverse energy gap between the two lowest-energy states of H_2^+ along the characteristic target-projectile separation during the scattering process. In Fig. 3(f) we calculate the probability that the target electron unbinds from the parent nucleus. As we choose a nuclear tunneling closer to the electronic component ($J_n/J_e > 0.1$), the kinetic energy of the projectile greatly exceeds the ionization energy of the target electron ($K_p/I \gg 100$), observing that the associated short interaction time suppresses further ionization events.

Simulating inelastic ionization.— Now, we investigate the case in which an electron is launched against a target hydrogen atom. For now, we consider that the electrons involved have opposite spin, so that they are distinguish-

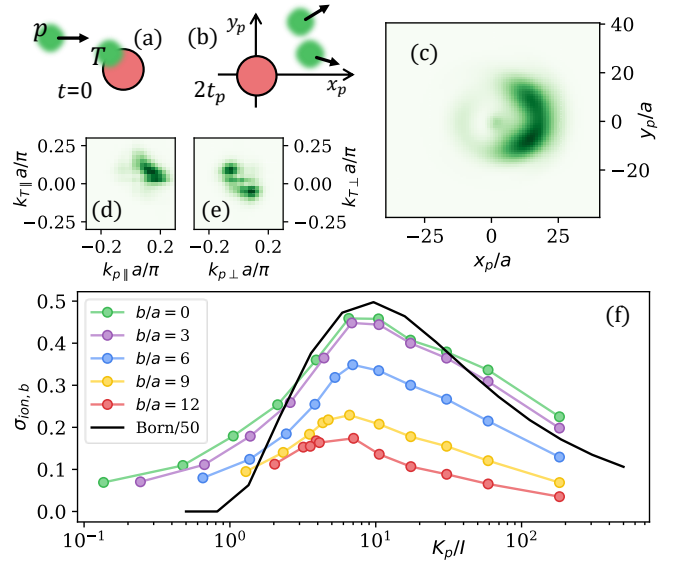


Figure 4. (a,b) Scheme of the electronic scattering against simulated hydrogen at initial and final time $2t_p$, respectively. (c) Projectile probability density at time $2t_p$, conditioned to the ionization of the target. (d,e) Momentum correlations between the projectile [p] and target [T] electron at time $2t_p$ along the incident direction and the orthogonal axis, respectively. (f) Total double ionization cross section for distinguishable particles for a single scattering event with impact factor b . Parameters: $V_0/J_e = 1$, $w_0/a = 3$, $r_0/a = 1.5$, $N_{x,y} = 80$.

able particles, and that the nuclear potential is fixed [see the scheme in Figs. 4(a,b)]. Now that the target and projectile electrons have the same simulated mass, they present the same tunneling rate J_e , which forces us to control the incoming kinetic energy K_p through the carrier wavevector k_0 . In Fig. 4(c) we show the scattered electron at final time $2t_p$. As confirmed in Figs. 4(d,e), when the target electron is ejected by the incoming projectile, both electrons are mostly emitted in the forward direction, while an anticorrelated momentum in the orthogonal axis is caused by their electronic repulsion.

The ionization rate can be calculated as the probability that the electron is ejected from the target atom. In Fig. 4(f) we show the ionization cross section as a function of the impact parameter for different values of the incoming kinetic energy, defined by the momentum of the wavepacket. For incoming energies below the ionization threshold, I , no ionization occurs. In the opposite limit, $K_p \gg I$, the short interaction time greatly reduces scattering events and ionization is suppressed. Therefore, the maximum ionization cross section corresponds to $K_p \sim I$, and we observe qualitative agreement with the result provided by the Born approximation for the total ionization cross section, integrated over all possible impact parameters (black line, see [49]).

Conclusions & outlook.— To sum up, we have shown

that ultracold molecules moving in two-dimensional optical lattices can be used to simulate simplified chemistry models where both the electronic and nuclear degrees of freedom are preserved. In particular, we have observed that the natural cubic scaling of dipolar interactions enables one to access phenomena where the interactions among electrons and nuclei are relevant, as is the case of scattering events with electronic exchange or inelastic ionization. Compared with scattering experiments with real gases, the simulated dynamics occurs at a more favorable spatial and temporal scale that can be measured with atomic gas microscopy [4, 56]. We foresee that as the number of simulated particles increases, this unprecedented access to single-particle events can thus provide a complementary tool to understand and benchmark numerical methods in scattering regimes inaccessible by classical methods, as proposed in other fields such as lattice gauge theories [55, 57, 58]. Other relevant examples are molecular configurations with exceptional points that require one to analyze the geometric phase of individual trajectories [44–47]. Finally, while in this Letter electrons and nuclei are codified by different rotational levels of a molecule, one can also consider other alternatives, such as relying on different states of Rydberg atoms [59, 60].

Acknowledgements.— J.A.-L. acknowledges support from the Spanish Ministerio de Ciencia e Innovación (MCIN/AEI/10.13039/501100011033, Grant No. PID2023-147469NB-C21), and the Generalitat de Catalunya (Grant No. 2021 SGR 01411). A.G.-T. acknowledges support from the CSIC Research Platform on Quantum Technologies PTI-001, from Spanish projects PID2021-127968NB-I00 funded by MICIU/AEI/10.13039/501100011033/ and by FEDER Una manera de hacer Europa, and from the QUANTERA project MOLAR with reference PCI2024-153449 and funded MICIU/AEI/10.13039/501100011033 and by the European Union. J.I.C acknowledges funding from the project FermiQP of the Bildungsministerium für Bildung und Forschung (BMBF) as well as from the Munich Quantum Valley, which is supported by the Bavarian State Government with funds from the High tech Agenda Bayern Plus. We acknowledge useful discussions with Octavio Roncero and Arthur Christianen about the simulation of molecular dynamics.

* javier.arguello.luengo@upc.edu

† a.gonzalez.tudela@csic.es

- [1] M. Lewenstein, A. Sanpera, V. Ahufinger, B. Damski, A. Sen(De), and U. Sen, Ultracold atomic gases in optical lattices: Mimicking condensed matter physics and beyond, *Advances in Physics* **56**, 243 (2007).
- [2] C. Gross and I. Bloch, Quantum simulations with ultracold atoms in optical lattices., *Science (New York, N.Y.)* **357**, 995 (2017), 28883070.
- [3] I. Bloch, J. Dalibard, and S. Nascimbène, Quantum simulations with ultracold quantum gases, *Nature Physics* **8**, 267 (2012).
- [4] C. Gross and W. S. Bakr, Quantum gas microscopy for single atom and spin detection, *Nat. Phys.* **17**, 1316 (2021).
- [5] R. A. Hart, P. M. Duarte, T.-L. Yang, X. Liu, T. Paiva, E. Khatami, R. T. Scalettar, N. Trivedi, D. A. Huse, and R. G. Hulet, Observation of antiferromagnetic correlations in the hubbard model with ultracold atoms, *Nature* **519**, 211 (2015).
- [6] M. Boll, T. A. Hilker, G. Salomon, A. Omran, J. Nespolo, L. Pollet, I. Bloch, and C. Gross, Spin- and density-resolved microscopy of antiferromagnetic correlations in fermi-hubbard chains, *Science* **353**, 1257 (2016).
- [7] L. W. Cheuk, M. A. Nichols, K. R. Lawrence, M. Okan, H. Zhang, E. Khatami, N. Trivedi, T. Paiva, M. Rigol, and M. W. Zwierlein, Observation of spatial charge and spin correlations in the 2d fermi-hubbard model, *Science* **353**, 1260 (2016).
- [8] A. Mazurenko, C. S. Chiu, G. Ji, M. F. Parsons, M. Kanász-Nagy, R. Schmidt, F. Grusdt, E. Demler, D. Greif, and M. Greiner, A cold-atom fermi-hubbard antiferromagnet, *Nature* **545**, 462 (2017).
- [9] M. Xu, L. H. Kendrick, A. Kale, Y. Gang, G. Ji, R. T. Scalettar, M. Lebrat, and M. Greiner, Frustration- and doping-induced magnetism in a fermi-hubbard simulator, *Nature* **620**, 971 (2023).
- [10] H.-J. Shao, Y.-X. Wang, D.-Z. Zhu, Y.-S. Zhu, H.-N. Sun, S.-Y. Chen, C. Zhang, Z.-J. Fan, Y. Deng, X.-C. Yao, Y.-A. Chen, and J.-W. Pan, Antiferromagnetic phase transition in a 3d fermionic hubbard model, *Nature* **632**, 267 (2024).
- [11] C. S. Chiu, G. Ji, A. Bohrdt, M. Xu, M. Knap, E. Demler, F. Grusdt, M. Greiner, and D. Greif, String patterns in the doped hubbard model, *Science* **365**, 251 (2019).
- [12] D. Bourgund, T. Chalopin, P. Bojovi, H. Schmler, S. Wang, T. Franz, S. Hirthe, A. Bohrdt, F. Grusdt, I. Bloch, and T. A. Hilker, Formation of individual stripes in a mixed-dimensional cold-atom FermiHubbard system, *Nature* **637**, 57 (2025).
- [13] P. Sompet, S. Hirthe, D. Bourgund, T. Chalopin, J. Bibo, J. Koepsell, P. Bojović, R. Verresen, F. Pollmann, G. Salomon, C. Gross, T. A. Hilker, and I. Bloch, Realizing the symmetry-protected haldane phase in fermi-hubbard ladders, *Nature* **606**, 484 (2022).
- [14] S. Hirthe, T. Chalopin, D. Bourgund, P. Bojović, A. Bohrdt, E. Demler, F. Grusdt, I. Bloch, and T. A. Hilker, Magnetically mediated hole pairing in fermionic ladders of ultracold atoms, *Nature* **613**, 463 (2023).
- [15] T. Hartke, B. Oreg, C. Turnbaugh, N. Jia, and M. Zwierlein, Direct observation of nonlocal fermion pairing in an attractive fermi-hubbard gas, *Science* **381**, 82 (2023).
- [16] M. Schreiber, S. S. Hodgman, P. Bordia, H. P. Lschen, M. H. Fischer, R. Vosk, E. Altman, U. Schneider, and I. Bloch, Observation of many-body localization of interacting fermions in a quasirandom optical lattice, *Science* **349**, 842 (2015).
- [17] M. A. Nichols, L. W. Cheuk, M. Okan, T. R. Hartke, E. Mendez, T. Senthil, E. Khatami, H. Zhang, and M. W. Zwierlein, Spin transport in a mott insulator of ultracold fermions, *Science* **363**, 383 (2019).
- [18] E. Guardado-Sanchez, A. Morningstar, B. M. Spar, P. T.

- Brown, D. A. Huse, and W. S. Bakr, Subdiffusion and heat transport in a tilted two-dimensional fermi-hubbard system, *Phys. Rev. X* **10**, 011042 (2020).
- [19] S. Scherg, T. Kohlert, P. Sala, F. Pollmann, B. Hebbe Madhusudhana, I. Bloch, and M. Aidelsburger, Observing non-ergodicity due to kinetic constraints in tilted fermi-hubbard chains, *Nature Communications* **12**, 4490 (2021).
- [20] M. C. Bañuls, R. Blatt, J. Catani, A. Celi, J. I. Cirac, M. Dalmonte, L. Fallani, K. Jansen, M. Lewenstein, S. Montangero, C. A. Muschik, B. Reznik, E. Rico, L. Tagliacozzo, K. Van Acoleyen, F. Verstraete, U.-J. Wiese, M. Wingate, J. Zakrzewski, and P. Zoller, Simulating lattice gauge theories within quantum technologies, *The European Physical Journal D* **74**, 165 (2020).
- [21] M. Aidelsburger, L. Barbiero, A. Bermudez, T. Chanda, A. Dauphin, D. González-Cuadra, P. R. Grzybowski, S. Hands, F. Jendrzejewski, J. Jünemann, G. Juzeliūnas, V. Kasper, A. Piga, S. J. Ran, M. Rizzi, G. Sierra, L. Tagliacozzo, E. Tirrito, T. V. Zache, J. Zakrzewski, E. Zohar, and M. Lewenstein, Cold atoms meet lattice gauge theory, *Philosophical Transactions of the Royal Society A* **380**, 20210064 (2022).
- [22] A. Di Meglio, K. Jansen, I. Tavernelli, C. Alexandrou, S. Arunachalam, C. W. Bauer, K. Borrás, S. Carrazza, A. Crippa, V. Croft, R. de Putter, A. Delgado, V. Dunjko, D. J. Egger, E. Fernández-Combarro, E. Fuchs, L. Funcke, D. González-Cuadra, M. Grossi, J. C. Halimeh, Z. Holmes, S. Kühn, D. Lacroix, R. Lewis, D. Lucchesi, M. L. Martinez, F. Meloni, A. Mezzacapo, S. Montangero, L. Nagano, V. R. Pascuzzi, V. Radescu, E. R. Ortega, A. Roggero, J. Schuhmacher, J. Seixas, P. Silvi, P. Spentzouris, F. Tacchino, K. Temme, K. Terashi, J. Tura, C. Tüysüz, S. Vallecorsa, U.-J. Wiese, S. Yoo, and J. Zhang, Quantum computing for high-energy physics: State of the art and challenges, *PRX Quantum* **5**, 037001 (2024).
- [23] J. Argüello-Luengo, A. González-Tudela, T. Shi, P. Zoller, and J. I. Cirac, Analogue quantum chemistry simulation, *Nature* **574**, 215 (2019).
- [24] J. Argüello-Luengo, A. González-Tudela, T. Shi, P. Zoller, and J. I. Cirac, Quantum simulation of two-dimensional quantum chemistry in optical lattices, *Physical Review Research* **2**, 042013 (2020).
- [25] J. Argüello-Luengo, T. Shi, and A. González-Tudela, Engineering analog quantum chemistry Hamiltonians using cold atoms in optical lattices, *Phys. Rev. A* **103**, 043318 (2021).
- [26] D. Malz and J. I. Cirac, Few-Body Analog Quantum Simulation with Rydberg-Dressed Atoms in Optical Lattices, *PRX Quantum* **4**, 020301 (2023).
- [27] R. J. MacDonell, C. E. Dickerson, C. J. Birch, A. Kumar, C. L. Edmunds, M. J. Biercuk, C. Hempel, and I. Kassel, Analog quantum simulation of chemical dynamics, *Chemical Science* **12**, 9794 (2021).
- [28] T. Navickas, R. J. MacDonell, C. H. Valahu, V. C. Olaya-Agudelo, F. Scuccimarra, M. J. Millican, V. G. Matsos, H. L. Nourse, A. D. Rao, M. J. Biercuk, C. Hempel, I. Kassel, and T. R. Tan, Experimental Quantum Simulation of Chemical Dynamics, *arXiv: 2409.04044* (2024).
- [29] C. H. Valahu, V. C. Olaya-Agudelo, R. J. MacDonell, T. Navickas, A. D. Rao, M. J. Millican, J. B. Pérez-Sánchez, J. Yuen-Zhou, M. J. Biercuk, C. Hempel, T. R. Tan, and I. Kassel, Direct observation of geometric-phase interference in dynamics around a conical intersection, *Nature Chemistry* **15**, 1503 (2023).
- [30] V. C. Olaya-Agudelo, B. Stewart, C. H. Valahu, R. J. MacDonell, M. J. Millican, V. G. Matsos, F. Scuccimarra, T. R. Tan, and I. Kassel, Simulating open-system molecular dynamics on analog quantum computers, *arXiv: 2407.17819* (2024).
- [31] J.-K. Ha and R. J. MacDonell, *Analog Quantum Simulation of Coupled Electron-Nuclear Dynamics in Molecules* (2024), *arXiv:2409.04427* [physics, physics:quant-ph].
- [32] L. Christakis, J. S. Rosenberg, R. Raj, S. Chi, A. Morningstar, D. A. Huse, Z. Z. Yan, and W. S. Bakr, Probing site-resolved correlations in a spin system of ultracold molecules, *Nature* **614**, 64 (2023).
- [33] B. Yan, S. A. Moses, B. Gadway, J. P. Covey, K. R. A. Hazzard, A. M. Rey, D. S. Jin, and J. Ye, Observation of dipolar spin-exchange interactions with lattice-confined polar molecules, *Nature* **501**, 521 (2013).
- [34] A. Chotia, B. Neyenhuis, S. A. Moses, B. Yan, J. P. Covey, M. Foss-Feig, A. M. Rey, D. S. Jin, and J. Ye, Long-Lived Dipolar Molecules and Feshbach Molecules in a 3D Optical Lattice, *Phys. Rev. Lett.* **108**, 080405 (2012).
- [35] J. M. Brown and A. Carrington, *Rotational Spectroscopy of Diatomic Molecules* (Cambridge University Press, 2003).
- [36] M. L. Wall, K. R. A. Hazzard, and A. M. Rey, Quantum magnetism with ultracold molecules (2015) pp. 3–37, *arXiv:1406.4758* [cond-mat].
- [37] A. Micheli, G. K. Brennen, and P. Zoller, A toolbox for lattice-spin models with polar molecules, *Nature Phys* **2**, 341 (2006).
- [38] A. V. Gorshkov, S. R. Manmana, G. Chen, J. Ye, E. Demler, M. D. Lukin, and A. M. Rey, Tunable Superfluidity and Quantum Magnetism with Ultracold Polar Molecules, *Phys. Rev. Lett.* **107**, 115301 (2011).
- [39] A. Micheli, G. Pupillo, H. P. Büchler, and P. Zoller, Cold polar molecules in two-dimensional traps: Tailoring interactions with external fields for novel quantum phases, *Phys. Rev. A* **76**, 043604 (2007).
- [40] M. L. Wall, *Hyperfine Molecular Hubbard Hamiltonian*, in *Quantum Many-Body Physics of Ultracold Molecules in Optical Lattices: Models and Simulation Methods*, edited by M. L. Wall (Springer International Publishing, Cham, 2015) pp. 93–119.
- [41] Z. Z. Yan, J. W. Park, Y. Ni, H. Loh, S. Will, T. Karman, and M. Zwierlein, Resonant Dipolar Collisions of Ultracold Molecules Induced by Microwave Dressing, *Phys. Rev. Lett.* **125**, 063401 (2020).
- [42] While the effective Hamiltonian holds valid for inter-site interactions, dipolar interactions will dominate over the electric field for separations $r < r_d \equiv (d^2/B_N)^3 \sim 10$ nm. As $r_d < a$, this will only affect on-site interactions, which motivates our choice of effective potential V_{mol} [41, 61]. Microwave shielding to repulsive resonant dipolar interactions could potentially be used to prevent molecules from getting closer to each other [41, 62].
- [43] A. Lombardi and F. Palazzetti, Chirality in molecular collision dynamics, *J. Phys.: Condens. Matter* **30**, 063003 (2018).
- [44] W. Domcke, H. Koppel, and D. R. Yarkony, *Conical Intersections: Electronic Structure, Dynamics & Spectroscopy* (World Scientific, 2004).
- [45] C. A. Mead and D. G. Truhlar, On the determination

- of Born–Oppenheimer nuclear motion wave functions including complications due to conical intersections and identical nuclei, *The Journal of Chemical Physics* **70**, 2284 (1979).
- [46] Y.-S. M. Wu and A. Kuppermann, Prediction of the effect of the geometric phase on product rotational state distributions and integral cross sections, *Chemical Physics Letters* **201**, 178 (1993).
- [47] S. C. Althorpe, F. Fernández-Alonso, B. D. Bean, J. D. Ayers, A. E. Pomerantz, R. N. Zare, and E. Wrede, Observation and interpretation of a time-delayed mechanism in the hydrogen exchange reaction, *Nature* **416**, 67 (2002).
- [48] A. Rubio-Abadal, J.-y. Choi, J. Zeiher, S. Hollerith, J. Rui, I. Bloch, and C. Gross, Many-Body Delocalization in the Presence of a Quantum Bath, *Phys. Rev. X* **9**, 041014 (2019).
- [49] See the End Matter accompanying this Letter for further details about engineering of the wavepacket, and the numerical benchmark of the proposal.
- [50] T. Fukuhara, A. Kantian, M. Endres, M. Cheneau, P. Schaus, S. Hild, D. Bellem, U. Schollwöck, T. Giamarchi, C. Gross, I. Bloch, and S. Kuhr, Quantum dynamics of a mobile spin impurity, *Nature Phys* **9**, 235 (2013).
- [51] M. Karski, L. Förster, J.-M. Choi, A. Steffen, W. Alt, D. Meschede, and A. Widera, Quantum Walk in Position Space with Single Optically Trapped Atoms, *Science* **325**, 174 (2009).
- [52] A. W. Young, W. J. Eckner, N. Schine, A. M. Childs, and A. M. Kaufman, Tweezer-programmable 2D quantum walks in a Hubbard-regime lattice, *Science* **377**, 885 (2022).
- [53] T. Lauber, P. Massignan, G. Birkl, and A. Sanpera, Atomic wave packet dynamics in finite time-dependent optical lattices, *J. Phys. B: At. Mol. Opt. Phys.* **44**, 065301 (2011).
- [54] C. M. Fabre, P. Cheiney, G. L. Gattobigio, F. Vermersch, S. Faure, R. Mathevet, T. Lahaye, and D. Guéry-Odelin, Realization of a Distributed Bragg Reflector for Propagating Guided Matter Waves, *Phys. Rev. Lett.* **107**, 230401 (2011).
- [55] G.-X. Su, J. Osborne, and J. C. Halimeh, *Cold-Atom Particle Collider*, *PRX Quantum* **5**, 040310 (2024).
- [56] C. Weitenberg, M. Endres, J. F. Sherson, M. Cheneau, P. Schaus, T. Fukuhara, I. Bloch, and S. Kuhr, Single-spin addressing in an atomic Mott insulator, *Nature* **471**, 319 (2011).
- [57] E. R. Bennowitz, B. Ware, A. Schuckert, A. Lerose, F. M. Surace, R. Belyansky, W. Morong, D. Luo, A. De, K. S. Collins, O. Katz, C. Monroe, Z. Davoudi, and A. V. Gorshkov, *Simulating Meson Scattering on Spin Quantum Simulators* (2024), arXiv:2403.07061.
- [58] V. Sharma and K. R. A. Hazzard, *Meson dynamics from locally exciting a particle-conserving Z2 lattice gauge theory* (2025), arXiv:2503.02791.
- [59] J. B. Balewski, A. T. Krupp, A. Gaj, S. Hofferberth, R. Löw, and T. Pfau, Rydberg dressing: Understanding of collective many-body effects and implications for experiments, *New J. Phys.* **16**, 063012 (2014).
- [60] E. Guardado-Sanchez, B. M. Spar, P. Schauss, R. Belyansky, J. T. Young, P. Bienias, A. V. Gorshkov, T. Iadecola, and W. S. Bakr, Quench Dynamics of a Fermi Gas with Strong Nonlocal Interactions, *Phys. Rev. X* **11**, 021036 (2021).
- [61] L. M. C. Janssen, *Cold Collision Dynamics of NH Radicals*, Ph.D. thesis, Radboud Universiteit Nijmegen (2012).
- [62] T. Karman, Z. Z. Yan, and M. Zwierlein, Resonant and first-order dipolar interactions between ultracold molecules in static and microwave electric fields, *Phys. Rev. A* **105**, 013321 (2022).
- [63] J. Blackledge and M. Rebow, Two-dimensional Schrodinger Scattering and Electron Transport in Graphene, *Articles* **10.21427/D7FW4Q** (2014).
- [64] I. R. Lapidus, Quantum-mechanical scattering in two dimensions, *American Journal of Physics* **50**, 45 (1982).
- [65] P. M. Morse and H. Feshbach, *Methods of Theoretical Physics* (Technology Press, 1946).
- [66] B. H. Bransden, *Atomic Collision Theory* (Benjamin/Cummings Publishing Company, Advanced Book Program, 1983).
- [67] G. Peach, Ionization of hydrogen, helium, lithium and beryllium by electron and proton impact, *Proceedings of the Physical Society* **85**, 709 (1965).
- [68] S. Lloyd, Universal quantum simulators, *Science* **273**, 1073 (1996).
- [69] A. M. Childs, Y. Su, M. C. Tran, N. Wiebe, and S. Zhu, Theory of Trotter Error with Commutator Scaling, *Phys. Rev. X* **11**, 011020 (2021).

END MATTER

Wavepacket engineering

In this Letter we have focused on the simulation of a scattering process where an incoming particle with initial momentum k_0 along the x-axis collides with a target species. First, let us consider that the projectile is a single particle (a nucleus or an electron), represented by the corresponding rotational level of a molecule. Initially, it is prepared in the spatially-gaussian ground state of width w_0 for a harmonic potential created, e.g. by an external optical potential. For a one-dimensional wavepacket to move towards its target, one can use a spatial-light modulator to imprint the needed site-dependent phase, which results into

$$\psi_{w_0, k_0}(x) = \frac{1}{(2\pi w_0^2)^{1/4}} e^{-\left(\frac{x-x_0}{2w_0}\right)^2} e^{ik_0 x}. \quad (\text{E1})$$

One should observe that, for the nearest-neighbor tunneling in Eq. (1), the dispersion relation for this wavepacket is of the form $\omega_x(k) = -2J \cos(k_0 a)$ and the maximum velocity is achieved for the carrier wavenumber $k_0 a = \pi/2$, whose group velocity is $v_g = 2Ja$. In addition to this linear region of the dispersion relation, the next terms of the dispersion relation around k_0 will introduce an unwanted skewness on the propagation that increases over time. For this effect to be controlled along the propagation time $t_p = s/v_g$ needed to reach the target at distance s , this translates into a minimal initial width for the wavepacket, $w_0/a \gtrsim (s/a)^{1/3}$. Under this condition, the state is initially localized in momentum, and the linear dispersion relation is a good approximation for the propagation of the wavepacket.

Moving now a two-dimensional configuration, the projectile will diffuse along the orthogonal axis due to the lowest-order quadratic expansion of $\omega(k)$. As a consequence, the width of the wavepacket, w_{J, k_0} increases over time, and an additional phase shift φ_{J, k_0} appears:

$$w_{J, k_0}(t) \approx w_0 \sqrt{1 + \frac{J^2 \cos^2(k_0 a) t^2 a^4}{w_0^4}}, \quad (\text{E2})$$

$$\varphi_{J, k_0}(x, t) \approx \frac{x^2}{4} \frac{J \cos(k_0 a) a^2 t}{w_0^4 + J^2 \cos^2(k_0 a) a^4 t^2}. \quad (\text{E3})$$

For 2D scattering trajectories of distance s , this distortion of the wavepacket in the direction orthogonal to the propagation may be undesirable, as one would like to preserve its symmetric shape when the collision occurs. To prevent this undesired expansion of the wavepacket, we initiate the simulation with self-focusing wavepackets that compensate for these additional effects

$$\psi_{\text{in}}(\mathbf{r}, 0) = \prod_{\sigma \in \{x, y\}} \psi_{w_{J, k_0 \sigma}(t_p), k_0 \sigma}(r_\sigma) e^{-i\varphi_{J, k_0 \sigma}(r_\sigma, t_p)}. \quad (\text{E4})$$

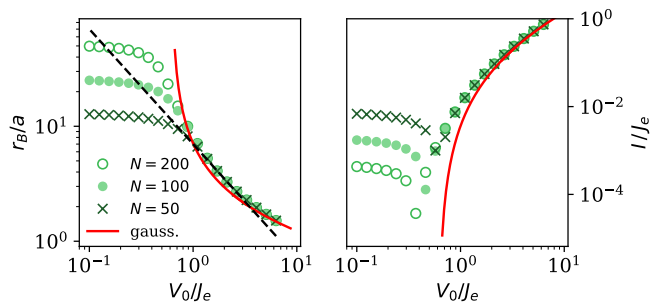


Figure E1. (a) Expected Bohr radius r_B , and (b) ionization energy I , for a simulated hydrogen atom with nuclear potential $V_{\text{mol}}(V_0, r)$ with $r_0/a = 1.5$, as a function of the potential strength V_0 and different values of the sites per side of the lattice N (see legend). Dashed line follows the scaling $r_B/a \propto J_e/V_0$, and red line shows the expectation for a gaussian ansatz.

Units mapping

The ionization energy (I) and the Bohr radius (r_B), define the natural energy and length scales of the simulated hydrogen atom, respectively. They are conveniently defined as the expected energy and radius of the electronic ground state: $I = -\langle H \rangle$ and $r_B = \sqrt{\langle r^2 \rangle}$.

In Fig. E1 we calculate I and r_B for the attractive nuclear potential, $V_{\text{mol}}(r)$, as a function of the ratio V_0/J_e for lattices with different numbers of sites. For $V_0 \ll J_e$, the electronic state spreads across the entire lattice and becomes sensitive to finite-size effects, where smaller lattices are more affected. In the opposite limit, one is more affected by the discretization of the lattice space. To further characterize this limit, one can consider gaussian states of the form $\psi_g(\mathbf{r}, w) = (\sqrt{\pi}w)^{-1} e^{-r^2/(2w^2)}$, to have an analytic approximation for the energy of the ground state as a function of the width w of the state. To obtain the red lines in Fig. E1, we numerically minimize the energy for the gaussian ansatz and the potential V_{mol} , where the optimal width satisfies $w_{\text{min}} = r_B$. For the chosen cutoff length, $r_0/a = 1.5$, we observe that the potential only allows one bound state, and that $r_B/a \sim 10$ is the maximum Bohr radius one can simulate in a lattice with $N_{x,y} \sim 100$ sites per side before finite-size effects appear, which corresponds to the choice $V_0 \sim J_e$ considered in Figs. 3 and 4.

Born approximation

After the scattering event, the outgoing state with momentum \mathbf{k} can write as $\psi(\mathbf{r}, \mathbf{k}) = \psi_{\text{in}}(\mathbf{r}) + \psi_{\text{sc}}(\mathbf{r}, \mathbf{k})$, where $\psi_{\text{in}}(\mathbf{r}) \sim e^{i\mathbf{k}_0 \mathbf{r}}$ is the incident wave, and the scattered wave can be expressed as a Born series whose lowest or-

der is [63]

$$\begin{aligned} \psi_{\text{sc}}(\mathbf{r}, \mathbf{k}) &= \int d\mathbf{r}' G_0(\mathbf{k}, \mathbf{r}, \mathbf{r}') V_{\text{mol}}(\mathbf{r}') \psi_{\text{in}}(\mathbf{r}') + \dots \\ &\rightarrow f(\theta) \frac{e^{i\mathbf{k}\mathbf{r}}}{\sqrt{r}}. \end{aligned} \quad (\text{E5})$$

The Born approximation only retains this lowest-order expansion of the interactions with the target. Heuristically, this is a good approximation provided that the time the incoming particle spends in the range of the potential is shorter than the time this potential needs to have a significant effect [$K_p \gg V_{\text{mol}}(s)$]. In our configuration, we use the 2-dimensional Green function [64, 65],

$$G_0(\mathbf{k}, \mathbf{r}, \mathbf{r}') = \frac{-1}{(2\pi)^2} \lim_{\epsilon \rightarrow 0} \int d\mathbf{k}' \frac{e^{i\mathbf{k}'(\mathbf{r}-\mathbf{r}')}}{k'^2 - k^2 - i\epsilon} = \frac{-i}{4} H_0^{(1)}(kd) \quad (\text{E6})$$

where $H_0^{(1)}(x)$ is the Hankel function of the first kind and $d = \mathbf{r} - \mathbf{r}'$. Expanding these expressions in the long distance limit $d \gg 1$, one finds the Born approximation for the scattering amplitude introduced in Eq. (E5),

$$f(\theta) \approx -\sqrt{\frac{1}{8k\pi}} e^{i\pi/4} \int d\mathbf{r}' e^{i(\mathbf{k}_0 - \mathbf{k})\mathbf{r}'} V_{\text{mol}}(V_0, r'). \quad (\text{E7})$$

To calculate the ionization cross section in Fig. 4(f), one must capture the correlations between the incoming and ejected electrons, whose final momenta \mathbf{k} and \mathbf{q} are related by energy conservation [66, 67] ($k^2 = k_0^2 + 2I - q^2$). The total ionization writes as,

$$\sigma_{\text{ion}} = \int_0^{2\pi} d\phi \int_0^{q_{\text{max}}} dq q \frac{k(q)}{k_0} \int d\theta |f_I(\mathbf{q}, \mathbf{k})|^2, \quad (\text{E8})$$

where ϕ, θ are the polar angles of \mathbf{q} and \mathbf{k} , respectively, and $q_{\text{max}} = \sqrt{k_0^2 + 2I}$ is the maximum momentum of the ejected electron. Here, $f_I(\mathbf{q}, \mathbf{k})$ is the 2-electron scattering amplitude associated to ionization. Following the Born approximation and approximating that both electrons screen each other, it simplifies as [66],

$$f_I(\mathbf{q}, \mathbf{k}) = \int d\mathbf{r}_2 e^{-i\mathbf{r}_2(\mathbf{q}-\Delta)} \psi_g(\mathbf{r}_2, r_B) \int d\mathbf{s} e^{i\Delta\mathbf{s}} V_{\text{mol}}(\mathbf{s}) \quad (\text{E9})$$

where $\mathbf{s} = \mathbf{r}_1 - \mathbf{r}_2$, and $\Delta = \mathbf{k} - \mathbf{k}_0$. One can see that the second integral corresponds to the Born scattering amplitude in Eq. E7, while the first integral is the Fourier transform of the target bound-electron, which we approximate by the gaussian ansatz introduced in the section *Units mapping*. Following Eq. (E8), these results are numerically integrated to obtain the Born expectation for the total ionization cross section shown in Fig. 4(f) as a black line.

Numerical methods

To numerically calculate the temporal evolution of the incoming self-focusing wavepacket (E4) and its in-

teraction with the target molecule, we use the split method [68, 69]. In this approach, we take advantage of the fact that the first line in Hamiltonian (1) (\hat{H}_k) is diagonal in momentum space, while the second line is diagonal in real space (\hat{H}_r). The evolution under the total Hamiltonian $\hat{H} = \hat{H}_k + \hat{H}_r$ is then Trotterized in short temporal intervals τ as,

$$e^{-i\hat{H}t} = \prod_{i=1}^{n=t/\tau} \left(e^{-i\hat{H}_r\tau} e^{-i\hat{H}_k\tau} \right) + \mathcal{O}\left(\tau^2 n |[\hat{H}_r, \hat{H}_k]|\right).$$

Before applying each evolution operator, one can then perform a fast Fourier transformation of the evolving state to conveniently express it in the appropriate real or momentum basis. This strategy highly reduces the computational cost of the operation, as both the state and operators have the size of the Hilbert space (as compared with the quadratic size that operators would require in an inconvenient basis). In this work, we have used $J_e\tau = 0.5$, where convergence is observed until the final time $2t_p$. The ionization rate in Fig. 3(f) corresponds to the probability that this final state is orthogonal to both the bound target and the unscattered projectile.

To extract numerically the differential cross section once the final time $2t_p$ is reached, we subtract the contribution of the freely propagating wavepacket from the evolved state to calculate the scattering wavefunction $\psi_{\text{sc},b}(\mathbf{r})$. We then calculate the overlap of the resulting density probability $|\psi_{\text{sc},b}|^2$ with angular probe functions $P_b(\theta_0, \Delta\theta) = \langle \psi_{\text{sc},b} | e^{-(\theta-\theta_0)^2/\Delta\theta^2} | \psi_{\text{sc},b} \rangle$ to extract the probability of the projectile to be scattered an angle θ after hitting the target. Compared with this single-trajectory simulation, the differential cross section $d\sigma(\theta)/d\theta$ is obtained in conventional scattering experiments from an incident flux \mathcal{J} , where the total number of detections depends on the number of incoming particles, $\mathcal{J}\Delta b$, so $N_b(\theta, \Delta\theta) = \Delta b \cdot \mathcal{J} \cdot P_b(\theta)$. To extract this average cross section from the simulator, we repeat the calculation for N_b values of impact parameters b_i , spaced by distance Δb to obtain the mapping

$$\frac{d\sigma(\theta)}{d\theta} = \frac{\sum_i N_{bi}(\theta, \Delta\theta)}{\Delta\theta \cdot \mathcal{J}} = \frac{\Delta b}{\Delta\theta} \sum_i P_{b_i}(\theta_0, \Delta\theta). \quad (\text{E10})$$

To calculate the total scattering cross section associated to ionization represented in Fig. 4(f), we average the result of Eq. (E10) with a probe width $\Delta\theta = 0.01$ over 31 values of θ uniformly distributed between 0 and 2π , and 6 values of b between 0 and $12a$. There, only the density probability where both electrons are separated from the fixed nucleus more than r_B is included, ensuring that inelastic ionization has occurred.